


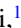





Excitonic effects in graphene-like C_3N Miki Bonacci ^{1,2,*} Matteo Zanfrognini ^{1,2} Elisa Molinari ^{1,2} Alice Ruini ^{1,2} Marilia J. Caldas ³
Andrea Ferretti ² and Daniele Varsano ^{2,†}¹*Dipartimento di Scienze Fisiche, Informatiche e Matematiche, Università di Modena e Reggio Emilia, I-41125 Modena, Italy*²*Centro S3, CNR-Istituto Nanoscienze, I-41125 Modena, Italy*³*Instituto de Física, Universidade de São Paulo, Cidade Universitária, 05508-900 São Paulo, Brazil*

(Received 16 November 2021; accepted 8 March 2022; published 23 March 2022)

Monolayer C_3N is an emerging two-dimensional indirect band gap semiconductor with interesting mechanical, thermal, and electronic properties. In this paper we present a description of C_3N electronic and dielectric properties, focusing on the so-called momentum-resolved exciton band structure. Excitation energies and oscillator strengths are computed in order to characterize bright and dark states, and discussed also with respect to the crystal symmetry. Activation of excitonic states is observed for finite transferred momenta: Indeed, we find an active indirect exciton at ~ 0.9 eV, significantly lower than the direct optical gap of 1.96 eV, with excitonic binding energies in the range 0.6–0.9 eV for the lowest states. As for other 2D materials, we find a quasilinear excitonic dispersion close to Γ , which however shows a downward convexity related to the indirect band gap of C_3N as well as to the dark nature of the involved excitons.

DOI: [10.1103/PhysRevMaterials.6.034009](https://doi.org/10.1103/PhysRevMaterials.6.034009)

I. INTRODUCTION

Since the rise of graphene [1,2], two-dimensional (2D) materials attract ever increasing attention in materials science. The reduced dimensionality and high surface-volume ratio affect all the properties of these systems leading to unique features. For example, graphene is well known for its superior mechanical stability [3] and electron mobility [4], relevant for applications in optoelectronics, sensing, mechanical and energy storage technologies [5–7]. However, graphene is a zero band gap semimetal, which limits its real application in digital electronic devices that usually require a semiconducting character. Hence the great effort, from both theoretical and experimental communities, to find postgraphene layered materials with a finite band gap appropriate for the selected applications. The list of candidates is very large [8] and includes, among others, transition metal dichalcogenides [9], phosphorene [10], and hexagonal boron nitride [11].

Carbon nitrides C_xN_y (e.g., CN, C_2N , C_3N , or C_3N_4) are gaining significant attention in recent years [12]. These are metal-free carbon-based layered materials with comparable (or even superior) structural, chemical, and electronic properties with respect to graphene. While preserving structural affinities with graphene, they generally display a semiconducting behavior. One of the most studied materials in this class is graphitic- C_3N_4 [13], as its strong optical absorption in the visible makes it suitable for solar energy conversion and photocatalysis applications [14]. Recently, a new carbon nitride, C_3N (structurally analogous to graphene and also known as 2D-polyaniline; see Fig. 1), an indirect gap semiconductor, has been experimentally synthesized using different

methods [15,16]. Since then, several studies were undertaken to characterize it. Theoretical investigations have shown that monolayer C_3N displays interesting features: remarkable mechanical properties, similar to graphene [17,18], high stability at room temperature and high thermal conductivity [19,20]. Moreover, it seems a promising material for acting as anode for Li-, Na-, and K-ion batteries [21–24]. It was also studied in heterostructures with graphene [18], C_3B [25], and g- C_3N_4 [26], showing interesting properties for optoelectronic and electrochemical energy storage devices.

Despite these interesting features, an extended characterization of excitations, including excitonic effects, in monolayer C_3N is still lacking. This knowledge would be relevant when considering C_3N for optoelectronic applications like photocatalysis, photodetection, solar cells, or light emitting diodes. Since the system is a 2D monolayer, the electronic screening is strongly reduced, implying that the enhanced electron-hole interaction typically leads to large excitonic binding energies (EBE) for all the relevant excitons. In a complementary direction, as discussed by Qiu *et al.* [27] and Cudazzo *et al.* [28], the study of the excitonic dispersion with respect to the transferred momentum \mathbf{q} can give more information on the excitonic features, in particular for low-dimensional systems. Moreover, it may have implications in plasmon/phonon-exciton coupling phenomena and can help in the determination of the exciton propagation along the crystal, relevant for excitation energy transport in the material [29]. In this paper we employ many-body perturbation theory methods in the GW approximation [30,31] and the Bethe Salpeter equation (BSE) [32] to study C_3N . In addition to a full characterization of the electronic and optical properties of this system, the excitonic band structure is computed in order to understand the exciton dispersion beyond the long wavelength limit. Specifically, momentum-dependent excitonic wave functions are also computed and discussed.

*Corresponding author: miki.bonacci@unimore.it†Corresponding author: daniele.varsano@nano.cnr.it

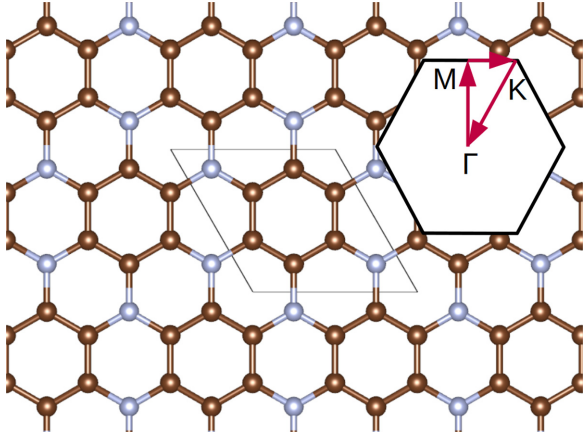


FIG. 1. Lattice structure of C_3N , with the corresponding unit cell. Brown and grey spheres represent the C and N atoms respectively. Inset: Brillouin zone with the k path considered in this paper.

II. METHODS

Ground-state electronic structure properties were calculated in the framework of density functional theory (DFT), using a plane wave basis set and pseudopotential approach as implemented in the Quantum ESPRESSO package [33,34]. We used optimized norm-conserving Vanderbilt (ONCV) pseudopotentials [35] to compute the relaxed structure and the corresponding Kohn-Sham (KS) single-particle energies and electronic density. The KS-DFT exchange-correlation functional was approximated using GGA-PBE [36]. The KS electronic structure was converged using a plane wave kinetic energy cutoff energy of 60 Ry to represent the wave functions, and a Monkhorst-Pack \mathbf{k} -point grid of $8 \times 8 \times 1$. We verified that a supercell with a vacuum of 15 Å along the vertical direction was enough to treat the system as 2D, avoiding spurious interactions between layers.

The KS energies are then corrected using many-body perturbation theory methods. In particular, we adopted the GW approximation [31] in the single shot G_0W_0 approach, and then computed the excitonic properties by solving the BSE [32]. GW and BSE calculations were performed using the Yambo code [37,38]. In the GW approximation, the expectation values of the self-energy are written as

$$\Sigma_{n\mathbf{k}}(\omega) = - \int \frac{d\omega'}{2\pi i} e^{i\omega'0^+} \langle n\mathbf{k} | G(\omega + \omega') W(\omega') | n\mathbf{k} \rangle, \quad (1)$$

where G is taken here as the Green's function built on single particle KS orbitals (and their corresponding eigenvalues $\epsilon_{n\mathbf{k}}$) and W is the screened Coulomb interaction calculated in the random phase approximation (RPA) with the frequency dependence treated via the Godby-Needs plasmon-pole model [39]. Quasiparticle energies were then obtained by solving the linearized equation

$$E_{n\mathbf{k}}^{\text{qp}} = \epsilon_{n\mathbf{k}} + Z_{n\mathbf{k}} [\Sigma_{n\mathbf{k}}(\epsilon_{n\mathbf{k}}) - v_{n\mathbf{k}}^{\text{xc}}], \quad (2)$$

where $v_{n\mathbf{k}}^{\text{xc}}$ is the expectation value of the exchange-correlation potential over the $n\mathbf{k}$ KS eigenvectors, and $Z_{n\mathbf{k}}$ is the

renormalization factor

$$Z_{n\mathbf{k}} = \left[1 - \left. \frac{\partial \Sigma_{n\mathbf{k}}(\omega)}{\partial \omega} \right|_{\omega=\epsilon_{n\mathbf{k}}} \right]^{-1}. \quad (3)$$

In all the calculations we used a truncated Coulomb potential [40] in order to avoid spurious interaction between repeated cells.

Converged quasiparticle energies were obtained using a kinetic energy cutoff of 10 Ry to represent the screening matrix, including 300 empty states in the sums over transitions and adopting a \mathbf{k} -point grid of $30 \times 30 \times 1$. Convergence on screening matrix cutoff and empty states is reached by means of automated workflows as implemented in the current version of the AiiDA-Yambo plugin [38] of the AiiDA software [41], imposing a convergence threshold of 15 meV. More details on the convergence workflow are provided in the Supplemental Material [42].

The quasiparticle energies were then inserted in the BSE. The excitonic Hamiltonian H^{exc} was built [31,43] considering a transferred momentum $\mathbf{q} = \mathbf{k}_c - \mathbf{k}_v$ between valence and conduction states, and reads (in the resonant block):

$$\langle v\mathbf{c}\mathbf{k}, \mathbf{q} | H^{\text{exc}} | v'\mathbf{c}'\mathbf{k}', \mathbf{q} \rangle = (E_{c',\mathbf{k}'}^{\text{qp}} - E_{v',\mathbf{k}'-\mathbf{q}}^{\text{qp}}) \delta_{v\mathbf{c}\mathbf{k}, v'\mathbf{c}'\mathbf{k}'} + \langle v\mathbf{c}\mathbf{k}, \mathbf{q} | v - W | v'\mathbf{c}'\mathbf{k}', \mathbf{q} \rangle, \quad (4)$$

where $|v\mathbf{c}\mathbf{k}, \mathbf{q}\rangle \equiv |c, \mathbf{k}\rangle \otimes |v, \mathbf{k} - \mathbf{q}\rangle$, $|v, \mathbf{k} - \mathbf{q}\rangle$ and $|c, \mathbf{k}\rangle$ being valence and conduction wave-functions, respectively. Concerning the kernel, W and v are the (screened) direct and (bare) exchange e-h interactions. The BSE can then be recast in the form of a two-particle eigenproblem for the excitonic eigenvalues $E^S(\mathbf{q})$ and eigenstates $|S, \mathbf{q}\rangle$:

$$H^{\text{exc}}(\mathbf{q}) |S, \mathbf{q}\rangle = E^S(\mathbf{q}) |S, \mathbf{q}\rangle \quad (5)$$

$$|S, \mathbf{q}\rangle = \sum_{v\mathbf{c}, \mathbf{k}} A_{v\mathbf{c}\mathbf{k}}^S(\mathbf{q}) |v\mathbf{c}\mathbf{k}, \mathbf{q}\rangle. \quad (6)$$

It is worth noticing that the \mathbf{q} index makes the BSE block diagonal: for different values of the transferred momentum we have different excitonic Hamiltonians $H^{\text{exc}}(\mathbf{q})$. Then, the excitonic band structure is calculated by solving the eigenvalue problem in Eq. (5) for each \mathbf{q} along a path. In this work the BSE was solved for several values of \mathbf{q} along the Γ - M and Γ - K directions.

It is also possible to define the inverse macroscopic dielectric function (considering only resonant and antiresonant parts of the H^{exc}) as

$$\epsilon_M^{-1}(\omega, \mathbf{q}) = 1 + \frac{2}{VN_q} v(\mathbf{q}) \sum_S \Omega^S(\mathbf{q}) \times \left[\frac{1}{E^S(\mathbf{q}) - (\omega + i\eta)} + \frac{1}{E^S(\mathbf{q}) + (\omega + i\eta)} \right], \quad (7)$$

where V is the volume of the unit cell and N_q is the number of points in the Brillouin zone (BZ) sampling. In the above equation, $\Omega^S(\mathbf{q})$ are the generalized oscillator strengths, defined as

$$\Omega^S(\mathbf{q}) = \left| \sum_{v\mathbf{c}, \mathbf{k}} A_{v\mathbf{c}\mathbf{k}}^S(\mathbf{q}) \langle v, \mathbf{k} - \mathbf{q} | e^{-i\mathbf{q}\cdot\mathbf{r}} | c, \mathbf{k} \rangle \right|^2. \quad (8)$$

Oscillator strengths are used to distinguish between active and inactive excitons (in the $\mathbf{q} = 0$ limit, in particular, to identify those that are dipole active/forbidden). Experimentally, excitonic effects are observed via photoabsorption spectroscopy in the optical limit of vanishing \mathbf{q} , while nonvanishing momentum excitations are observed, e.g., in electron energy loss spectroscopy (EELS) or nonresonant inelastic x-ray scattering (NRIXS) experiments, by measuring the loss function $L(\omega, \mathbf{q})$ [31]. The optical absorption and the loss function are related to the inverse of the macroscopic dielectric matrix $\epsilon_M^{-1}(\omega, \mathbf{q})$ by the relations:

$$\text{Abs}(\omega, \mathbf{q} \rightarrow 0) = \text{Im} \left[\frac{1}{\epsilon_M^{-1}(\omega, \mathbf{q} \rightarrow 0)} \right], \quad (9)$$

$$L(\omega, \mathbf{q}) = -\text{Im}[\epsilon_M^{-1}(\omega, \mathbf{q})]. \quad (10)$$

In EELS and NRIXS experiments, the measured quantity is the intensity of the scattered particles resolved with respect to the scattering angle and to the energy of the outgoing particles (either electrons or photons). This quantity, that is the differential cross section $\frac{d^2\sigma}{d\Omega dE}$ of the process, can be related to the loss function by the relation [44,45]:

$$\frac{d^2\sigma}{d\Omega dE} \sim \begin{cases} q^{-2}L(\omega, \mathbf{q}) & \text{EELS,} \\ q^2L(\omega, \mathbf{q}) & \text{NRIXS.} \end{cases} \quad (11)$$

Computationally, in order to converge BSE calculations for C₃N, we used a \mathbf{k} -point mesh of $64 \times 64 \times 1$. To numerically represent and solve the eigenproblem of Eq. (4) we verified that three valence and three conduction bands are enough to obtain converged excitation energies for the first excitons within 10 meV.

III. RESULTS AND DISCUSSION

Electronic properties. C₃N has a honeycomb lattice, with a unit cell composed of 6 carbon and 2 nitrogen atoms, as shown in Fig. 1. Like graphene, it assumes a planar and continuously bonded geometry, due to the character of the sp^2 hybridized orbitals. For monolayer C₃N we find a relaxed lattice constant of 4.857 Å (using GGA-PBE). This result agrees well with previous DFT calculations (4.862 Å) [46] and is slightly larger than the experimental value (4.75 Å) [15]. The KS band structure [Fig. 2(a)] shows a Dirac cone at the K point. Now, since C₃N has two more electrons per unit cell than graphene, the level-filling goes up and the Dirac cone is no longer at the valence-band top. The calculated band gap is indirect ($M \rightarrow \Gamma$) and amounts to 0.42 eV (at the GGA-PBE level). The direct gaps at Γ and M are 1.86 eV and 1.61 eV, respectively. Figure 2(a) highlights also the σ and π character of the bands in the gap region, and we can observe that the top valence bands show π symmetry as well as the two lowest conduction bands, whereas σ -like character is seen in the third and the fourth conduction bands (which start above ~ 2 eV with respect to the top valence band).

The inclusion of GW corrections provides a gap opening of ~ 1 eV, resulting in an indirect quasiparticle band gap of 1.42 eV [Fig. 2(b)]. The direct gaps at Γ and M are also increased to 2.96 and 2.67 eV, respectively, as summarized in Table I. The minimum direct gap is located in the middle of the Γ - M region of the BZ and has a value of 2.62 eV. The

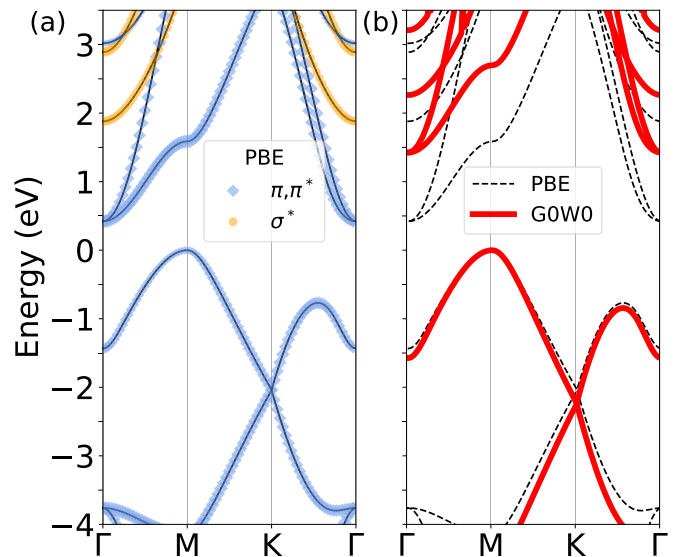


FIG. 2. (a) Orbital projected PBE band structure. π and π^* bands are indicated in blue, σ^* as orange dots. (b) G_0W_0 band structure (red); the corresponding PBE bands are reported again as dashed curves for reference. In both panels the zero of the energy scale is set at the top of the valence band for both PBE and G_0W_0 results.

GW band gap is consistent with the one obtained in a recent work by Wu *et al.* [47], calculated at the GW level using the Hybertsen-Louie generalized plasmon pole model [48], and as expected is larger than that obtained directly with the HSE06 hybrid functional [49], by ~ 0.38 eV [46]. The C₃N gap is narrower with respect to the two well-known carbon nitrides g-C₃N₄ (~ 4.24 eV for the triazine structure) [50] and C₂N (~ 3.75 eV) [51] single layers. This is consistent with the fact that C₃N is continuously bonded, while the two other carbon nitrides have saturated porous structure resulting in electronic confinement.

Along the same BZ path, the C₃N band structure calculated at GW level is qualitatively similar to the one calculated using PBE, as shown in Fig. 2(b). In fact, the GW gap is still indirect with the valence band maximum located at M and the conduction band minimum at Γ . We observe, anyhow, that the GW correction is not uniform across the bands, as different corrections apply due to wave functions with different character. Orbital-dependent GW corrections are a well-known feature of GW already discussed in the literature [52,53]. In particular, the corrections in the low conduction region are distinguished according to the different localization of the KS wave functions, as can be observed from Fig. 3, where the GW energies are plotted against the respective KS eigenvalues.

TABLE I. Indirect and direct energy gaps at high symmetry points obtained at PBE and G_0W_0 level.

| Gaps | PBE (eV) | G_0W_0 (eV) |
|-----------------------------|----------|---------------|
| $M \rightarrow \Gamma$ | 0.42 | 1.42 |
| $\Gamma \rightarrow \Gamma$ | 1.86 | 2.96 |
| $M \rightarrow M$ | 1.61 | 2.67 |

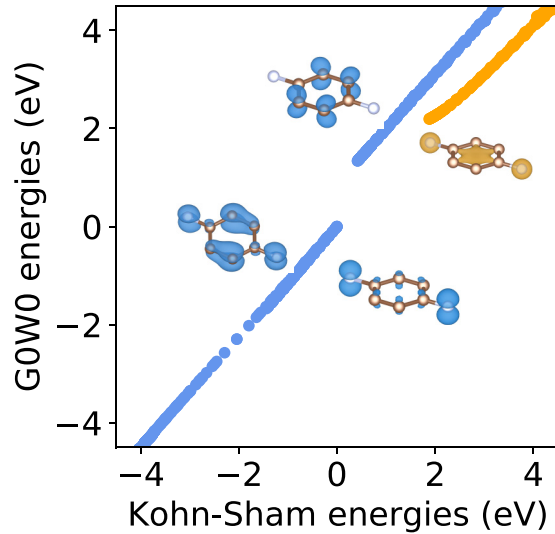


FIG. 3. Quasiparticle G_0W_0 energies vs Kohn-Sham PBE eigenvalues. The top of the valence band is chosen as a common zero of the energy. The colours and the corresponding insets indicate the predominant π , π^* (blue) and σ^* (orange) character. In the conduction region, two branches result from the different localization of the π^* - and σ^* -character states leading to different quasiparticle corrections.

A larger correction is observed for the bands with π^* (blue dots) character with respect to bands having σ^* character (orange dots). Since the valence bands considered here only present a π character (σ states are deeper in energy), their GW correction shows a more common scissor/stretching behavior. We note that this picture allows us to include the GW correction (for instance in the BSE calculations) as a generalized scissor and stretching operator, taking into account different corrections according to the specific localization character of the KS states.

Optical properties. The optical absorption, obtained from the $\mathbf{q} \rightarrow 0$ limit of the macroscopic dielectric response, according to Eq. (9), is shown in Fig. 4. Excitonic effects were included by solving the BSE equation. All the excitation energies are plotted, together with the independent-particle onset, at $E_{IP-GW} = 2.62$ eV, indicated by the vertical red line. The absorption spectrum is dominated by a main peak at 1.96 eV, originated by the doubly-degenerate exciton $E_0^{4,5}$. At lower energies, three dark excitons are present, the lowest ones (1.82 eV, $E_0^{1,2}$) being also doubly-degenerate.

Both bright and dark excitons are strongly bound, displaying EBE of 0.93 eV and 0.66 eV, for $E_0^{1,2}$ and $E_0^{4,5}$. The EBE are computed considering the difference between the excitation energy of the exciton and the average energy of the involved electron-hole transitions, as shown in the lower panel of Fig. 5. Interestingly, the EBE of the lowest bright exciton $E_0^{4,5}$ satisfies the scaling law $EBE \sim \frac{1}{4}E_{IP-GW}$, found valid for 2D single-layered systems [54,55].

In order to analyze the spatial extension of the main excitons, we plot their excitonic wave function, by showing the electron spatial distribution for a fixed hole position. The upper panel of Fig. 5 displays the excitonic wave function for the lowest ($E_0^{1,2}$) and the brightest ($E_0^{4,5}$) direct excitons,

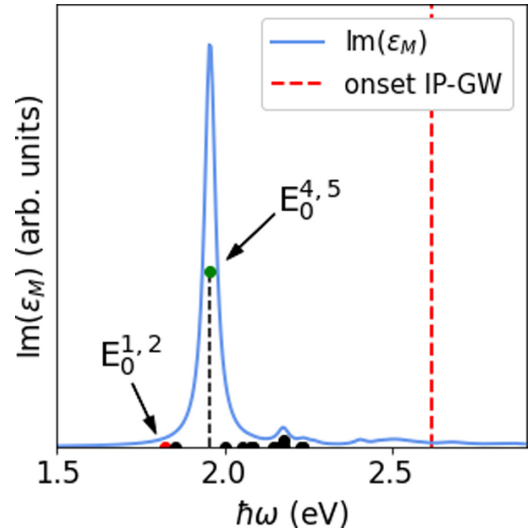


FIG. 4. Calculated $\text{Im}(\epsilon_M)$ in the optical limit ($\mathbf{q} \rightarrow 0$), in arbitrary units (arb. units). A Lorentzian broadening of 0.02 eV has been included. The dots indicate the amplitude of each excitonic state in the BSE solution. The vertical dashed red line represents the onset of the single quasiparticle continuum (minimum direct gap in the GW solution, 2.62 eV).

with the hole placed on a N site. Both excitons show a three-fold rotational plus a reflection symmetry with respect to the axis in the armchair direction. Interestingly, these excitons are localized on benzene rings, avoiding the N atoms. We observe that the dark excitons (lower energy) are strongly localized around the hole, while the active ones (higher energy)

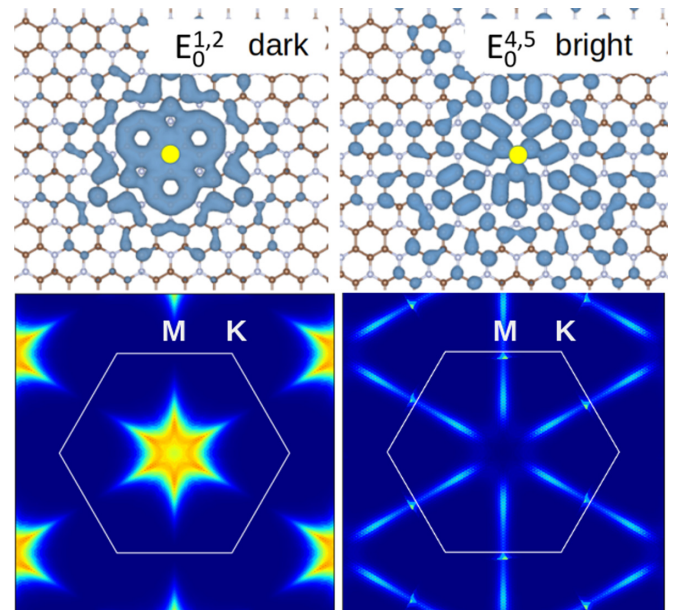


FIG. 5. Upper panels: Excitonic probability distribution for the dark $E_0^{1,2}$ and the bright (1.96 eV, $E_0^{4,5}$) excitons at vanishing \mathbf{q} . The blue contours represent the probability of finding the electron (hole) when the hole (electron) is fixed on a N atom (yellow circle). Lower panels: Distribution of the electron-hole transitions in the BZ for the corresponding excitons of the upper panels.

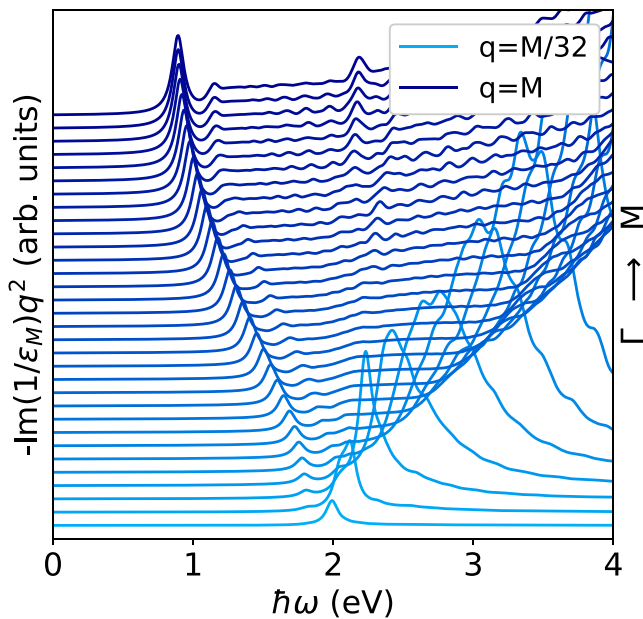


FIG. 6. Loss function for different values of the transferred momentum along the direction Γ - M , starting from the lowest $\mathbf{q} = M/32$ (light blue), to the highest $\mathbf{q} = M$ (dark blue). Following Cudazzo *et al.* [28], we multiplied all spectra by the corresponding q^2 . This is needed in order to enhance higher momentum spectra and physically motivated by the form of the NRIXS cross section (as discussed in Sec. II).

are more delocalized. We can explain the different spatial localization in terms of the single particle transitions that contribute to the excitations, as represented in the lower panels of Fig. 5. The first excitons $E_0^{1,2}$ are built from electron-hole transitions belonging to a larger region of the Brillouin zone with respect to $E_0^{4,5}$, resulting in a larger confinement in real space. Similarly to the fundamental gap, the optical gap of C₃N is also smaller than the ones calculated for g-C₃N₄ and C₂N (by about ~ 2 eV and ~ 1 eV [51], respectively, by considering the first bright excitons), which is consistent with a picture where the presence of saturated pores in each layer of the structure induces wave function localization and quantum confinement.

Indirect excitons. Besides the optical absorption limit, our understanding of electron-hole excitations in C₃N is further enhanced by inspecting the excitonic spectrum over a wider range of transferred momenta $\mathbf{q} = \mathbf{k}_{\text{elec}} - \mathbf{k}_{\text{hole}}$, providing us with the exciton dispersion in momentum space. Indeed, the excitonic dispersion was recently proposed [28] as a powerful tool to distinguish excitons of different character in low-dimensional systems, going beyond the mere evaluation of the EBE. The solution of the BSE for finite \mathbf{q} then allows us to fully characterize the C₃N excitations accessible by means of momentum-resolved electron energy loss spectroscopy or nonresonant inelastic x-ray scattering. Figure 6 shows the loss function calculated for different transferred momenta \mathbf{q} along the $\Gamma - M$ path. To compare spectra at different momentum, we multiplied the loss function by a q^2 factor. While making the plot more readable, this factor is also experimentally motivated by the form of the NRIXS cross section, as discussed in the theory section.

We observe that the low-energy peak goes down in energy for \mathbf{q} moving away from Γ , as expected for an indirect gap system. This indicates the presence of a dispersive excitonic band reaching a minimum of ~ 0.8 eV at $\mathbf{q} = M$ in correspondence of the indirect gap.

To complement the information provided by the loss spectra, in Fig. 7(a) we present the calculated \mathbf{q} -resolved exciton band structure. A color map is added to indicate the (generalized) amplitude/strength of each excitonic state, actually offering richer information complementary to the loss spectrum. The lowest degenerate exciton $E_0^{1,2}$ at Γ splits into two excitonic bands that we call E_q^1 and E_q^2 . For both $\Gamma - M$ and $\Gamma - K$ directions, we observe that the lowest excitons present quadratic and almost linear dispersions in the neighborhood of the Γ point, as also found for other 2D systems [27,28,56]. Nevertheless, at variance with what reported in the work of Qiu *et al.* [27] for the direct gap MoS₂ monolayer, here we find a lower band with quasilinear dependence on $|\mathbf{q}|$ and an upper band with a clear parabolic dispersion, both with a negative slope and concavity. Such a behavior is due to the indirect nature of the gap, and we note that—at difference with other 2D materials such as MoS₂ and phosphorene [29]—in the case of C₃N we do not observe a nonanalytical dispersion for the lowest bands. This is related to the fact that the $E_0^{1,2}$ excitons are dark, making the exchange contribution to the dispersion negligible. Moreover, the observed downward quasilinear behavior can be seen to be connected to the independent-particle contribution to the excitonic Hamiltonian, as shown in Fig. S2 in the Supplemental Material [42].

Moreover, the $\Gamma - M$ direction is of special interest, since it corresponds to \mathbf{q} vector involved in the indirect band gap: The most relevant excitonic transitions occur in that zone, and the decrease of excitation energies going from Γ to M reflects the indirect gap of C₃N. From Fig. 7(a) we observe that the lowest exciton (E_q^1) is inactive, with an energy minimum of 0.8 eV at $\mathbf{q} = M$. For this momentum, the immediately higher-energy exciton (0.9 eV, E_q^2) is active. Concerning the Γ - K path, we observe a minimum near $K/2$ that corresponds to an inactive state of energy ~ 1.3 eV. We find that EBE range from 0.6 eV to 0.93 eV for the lowest excitonic band in the Γ - M direction ($E_0^{1,2}$ - E_q^1). As we move out of the long-wavelength regime and choose given directions of the center-of-mass momentum \mathbf{q} , we expect some symmetries in the excitonic wave functions, like the three-fold rotational invariance observed in the plots of Fig. 5, to break. Figure 7(b) shows the square modulus of exciton wave functions (E_q^1 and E_q^2) at $\mathbf{q} = M$, corresponding to minima in the band structure of Fig. 7(a). As before, the hole is placed on a nitrogen atom. The threefold rotational symmetry is no longer present, and only the reflection invariance with respect to the armchair direction is maintained. Both E_q^1 and E_q^2 excitons are delocalized along the zig-zag direction. For the inactive excitons the symmetry axis lies on a nodal plane, where the probability amplitude of finding electrons vanishes. The spatial delocalization increases with \mathbf{q} and is higher for the indirect active exciton E_q^2 , as happens for the bright excitons in the optical limit case. The behavior of the excitonic wave function of C₃N is very similar to that observed in hBN by Sponza *et al.* [56]. This is because, along the armchair direction, both systems present the same

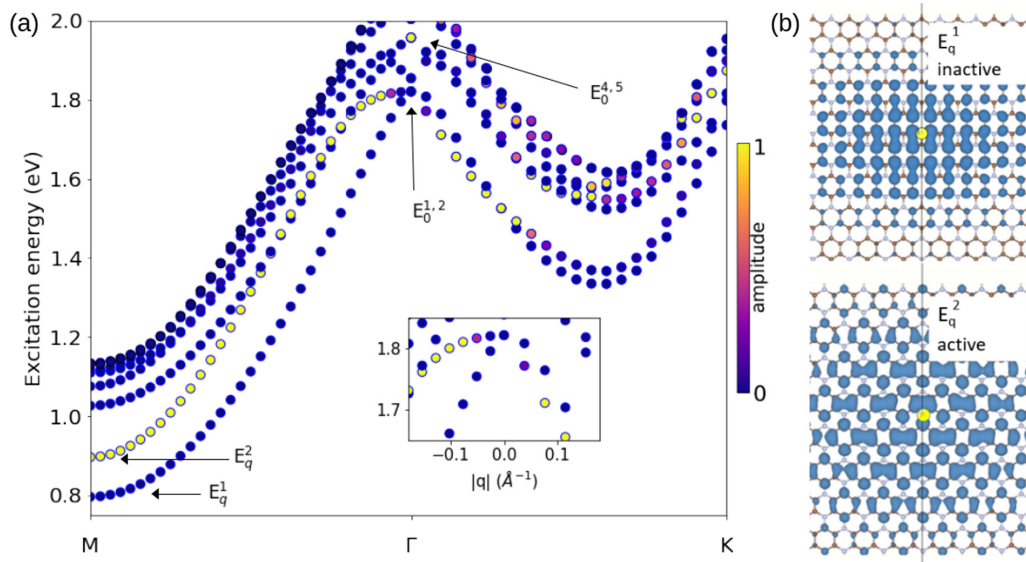


FIG. 7. (a) Momentum-resolved exciton band structure for the lowest seven excitons. Excitonic amplitudes are normalized with respect to the brightest exciton among all the bands for each momenta from dark violet to yellow (active exciton). Inset: Focus on the region near the $q = 0$ for the two lowest excitonic bands. (b) Exciton probability distribution for E_q^1 (top) and E_q^2 (bottom), at $\mathbf{q} = M$. The vertical solid line denotes the symmetry plane perpendicular to the figure and the hole position is indicated in yellow near the center of the figures.

reflection symmetry that characterizes the localization of excitons.

IV. CONCLUSIONS

In this paper we have studied the electronic and optical properties of single-layer C_3N by using *ab initio* methods based on DFT and many-body schemes. In particular, we have computed the 2D band structure of C_3N within the GW approximation, revealing an indirect quasiparticle band gap of 1.42 eV (top of the valence band located at M , bottom of the conduction band at Γ), with direct gaps at Γ and M of 2.96 and 2.67 eV, respectively. The GW corrections to quasiparticle energies were also discussed in view of the orbital symmetry and localization.

Neutral excitations, as those sampled by optical absorption ($\mathbf{q} = 0$) and electron energy loss spectroscopy (finite \mathbf{q}), are computed using the Bethe Salpeter equation. One of the main results of the work comes from the calculation of the full excitonic dispersion of C_3N in \mathbf{q} space, giving access to indirect excitons energies and intensities. These excitons play an important role in phonon-assisted photoluminescence [57,58], and they can be efficiently exploited for chemical sensing [59]. Interestingly, while the excitonic dispersion shows a parabolic behavior at M , corresponding to the indirect band

gap, at Γ we observe a degenerate doublet, which splits into a parabolic and a quasilinear dispersing bands, as for other 2D materials. A peculiarity of C_3N , connected with its indirect gap as well as with the dark nature of the excitons involved, is that the quasilinear band has downward convexity, at variance with MoS_2 or hBN and the quasilinear dispersion of the lower excitonic band comes from its independent-particle contribution. Finally, this paper represents a solid starting point to consider the role of excitonic effects of C_3N in more specific cases, e.g., in describing exciton-phonon scattering or the spectroscopy of in-plane adsorbates/defects.

ACKNOWLEDGMENTS

This work was partially funded by the EU through the MaX Centre of Excellence for HPC applications (Project No. 824143), and by Regione Emilia Romagna through a FSE PhD fellowship on Big data analysis & high performance simulations for materials. We also thank SUPER (Supercomputing Unified Platform – Emilia-Romagna) from Emilia-Romagna POR-FESR 2014-2020 Regional Funds. MJC acknowledges CNPq, FAPESP, and CAPES via the INCT-INEO Grant. We acknowledge PRACE for awarding us access to the Marconi100 system based in Italy at CINECA.

- [1] K. S. Novoselov, A. K. Geim, S. V. Morozov, D. Jiang, Y. Zhang, S. V. Dubonos, I. V. Grigorieva, and A. A. Firsov, *Science* **306**, 666 (2004).
 [2] K. S. Novoselov, A. K. Geim, S. V. Morozov, D. Jiang, M. I. Katsnelson, I. V. Grigorieva, S. V. Dubonos, and A. A. Firsov, *Nature (London)* **438**, 197 (2005).

- [3] A. E. Galashev and O. R. Rakhmanova, *Phys. Usp.* **57**, 970 (2014).
 [4] Y.-C. Lin, C. Jin, J.-C. Lee, S.-F. Jen, K. Suenaga, and P.-W. Chiu, *ACS Nano* **5**, 2362 (2011).
 [5] S. Das, J. A. Robinson, M. Dubey, H. Terrones, and M. Terrones, *Annu. Rev. Mater. Res.* **45**, 1 (2015).

- [6] S. J. Kim, K. Choi, B. Lee, Y. Kim, and B. H. Hong, *Annu. Rev. Mater. Res.* **45**, 63 (2015).
- [7] R. Zhang and R. Cheung, in *Two-Dimensional Materials*, edited by P. K. Nayak (IntechOpen, Rijeka, 2016), Chap. 10.
- [8] N. Mounet, M. Gibertini, P. Schwaller, D. Campi, A. Merkys, A. Marrazzo, T. Sohier, I. E. Castelli, A. Cepellotti, and G. Pizzi, *Nat. Nanotechnol.* **13**, 246 (2018).
- [9] Q. H. Wang, K. Kalantar-Zadeh, A. Kis, J. N. Coleman, and M. S. Strano, *Nat. Nanotechnol.* **7**, 699 (2012).
- [10] H. Liu, A. T. Neal, Z. Zhu, Z. Luo, X. Xu, D. Tománek, and P. D. Ye, *ACS Nano* **8**, 4033 (2014).
- [11] C. R. Dean, A. F. Young, I. Meric, C. Lee, L. Wang, S. Sorgenfrei, K. Watanabe, T. Taniguchi, P. Kim, K. L. Shepard *et al.*, *Nat. Nanotechnol.* **5**, 722 (2010).
- [12] D. Adekoya, S. Qian, X. Gu, W. Wen, D. Li, J. Ma, and S. Zhang, *Nano-Micro Letters* **13**, 13 (2021).
- [13] Y. Xu and S.-P. Gao, *Int. J. Hydrogen Energy* **37**, 11072 (2012).
- [14] A. Naseri, M. Samadi, A. Pourjavadi, A. Z. Moshfegh, and S. Ramakrishna, *J. Mater. Chem. A* **5**, 23406 (2017).
- [15] J. Mahmood, E. K. Lee, M. Jung, D. Shin, H.-J. Choi, J.-M. Seo, S.-M. Jung, D. Kim, F. Li, M. S. Lah *et al.*, *Proc. Natl. Acad. Sci. USA* **113**, 7414 (2016).
- [16] S. Yang, W. Li, C. Ye, G. Wang, H. Tian, C. Zhu, P. He, G. Ding, X. Xie, Y. Liu *et al.*, *Adv. Mater.* **29**, 1605625 (2017).
- [17] L.-B. Shi, Y.-Y. Zhang, X. Xiu, and H.-K. Dong, *Carbon* **134**, 103 (2018).
- [18] D. Wang, Y. Bao, T. Wu, S. Gan, D. Han, and L. Niu, *Carbon* **134**, 22 (2018).
- [19] B. Mortazavi, *Carbon* **118**, 25 (2017).
- [20] Y. Gao, H. Wang, M. Sun, Y. Ding, L. Zhang, and Q. Li, *Phys. E: Low-Dimens. Syst. Nanostructures* **99**, 194 (2018).
- [21] J. Xu, J. Mahmood, Y. Dou, S. Dou, F. Li, L. Dai, and J.-B. Baek, *Adv. Mater.* **29**, 1702007 (2017).
- [22] G.-C. Guo, R.-Z. Wang, B.-M. Ming, C. Wang, S.-W. Luo, M. Zhang, and H. Yan, *J. Mater. Chem. A* **7**, 2106 (2019).
- [23] Q. Liu, B. Xiao, J.-B. Cheng, Y.-C. Li, Q.-Z. Li, W.-Z. Li, X.-F. Xu, and X.-F. Yu, *ACS Appl. Mater. Interfaces* **10**, 37135 (2018).
- [24] P. Bhauriyal, A. Mahata, and B. Pathak, *J. Phys. Chem. C* **122**, 2481 (2018).
- [25] C. Zhang, Y. Jiao, T. He, S. Bottle, T. Frauenheim, and A. Du, *J. Phys. Chem. Lett.* **9**, 858 (2018).
- [26] J. Wang, X. Li, Y. You, X. Yang, Y. Wang, and Q. Li, *Nanotechnology* **29**, 365401 (2018).
- [27] D. Y. Qiu, T. Cao, and S. G. Louie, *Phys. Rev. Lett.* **115**, 176801 (2015).
- [28] P. Cudazzo, L. Sponza, C. Giorgetti, L. Reining, F. Sottile, and M. Gatti, *Phys. Rev. Lett.* **116**, 066803 (2016).
- [29] D. Y. Qiu, G. Cohen, D. Novichkova, and S. Refaely-Abramson, *Nano Lett.* **21**, 7644 (2021).
- [30] L. Hedin, *Phys. Rev.* **139**, A796 (1965).
- [31] G. Onida, L. Reining, and A. Rubio, *Rev. Mod. Phys.* **74**, 601 (2002).
- [32] G. Strinati, *La Rivista del Nuovo Cimento* (1978-1999) **11**, 1 (1988).
- [33] P. Giannozzi, S. Baroni, N. Bonini, M. Calandra, R. Car, C. Cavazzoni, D. Ceresoli, G. L. Chiarotti, M. Cococcioni, I. Dabo *et al.*, *J. Phys.: Condens. Matter* **21**, 395502 (2009).
- [34] P. Giannozzi, O. Andreussi, T. Brumme, O. Bunau, M. Buongiorno Nardelli, M. Calandra, R. Car, C. Cavazzoni, D. Ceresoli, M. Cococcioni *et al.*, *J. Phys.: Condens. Matter* **29**, 465901 (2017).
- [35] D. R. Hamann, *Phys. Rev. B* **88**, 085117 (2013).
- [36] J. P. Perdew, K. Burke, and M. Ernzerhof, *Phys. Rev. Lett.* **77**, 3865 (1996).
- [37] A. Marini, C. Hogan, M. Grüning, and D. Varsano, *Comput. Phys. Commun.* **180**, 1392 (2009).
- [38] D. Sangalli, A. Ferretti, H. Miranda, C. Attaccalite, I. Marri, E. Cannuccia, P. Melo, M. Marsili, F. Paleari, A. Marrazzo *et al.*, *J. Phys.: Condens. Matter* **31**, 325902 (2019).
- [39] R. W. Godby and R. J. Needs, *Phys. Rev. Lett.* **62**, 1169 (1989).
- [40] C. A. Rozzi, D. Varsano, A. Marini, E. K. U. Gross, and A. Rubio, *Phys. Rev. B* **73**, 205119 (2006).
- [41] S. P. Huber, S. Zoupanos, M. Uhrin, L. Talirz, L. Kahle, R. Häuselmann, D. Gresch, T. Müller, A. V. Yakutovich, C. W. Andersen *et al.*, *Sci. Data* **7**, 300 (2020).
- [42] See Supplemental Material at <http://link.aps.org/supplemental/10.1103/PhysRevMaterials.6.034009> for details on convergence studies for the GW results and for the analysis of the independent particle contribution in the BSE solution of the excitonic dispersion.
- [43] M. Gatti and F. Sottile, *Phys. Rev. B* **88**, 155113 (2013).
- [44] K. Sturm, *Zeitschrift für Naturforschung A* **48**, 233 (1993).
- [45] F. Fossard, L. Sponza, L. Schué, C. Attaccalite, F. Ducastelle, J. Barjon, and A. Loiseau, *Phys. Rev. B* **96**, 115304 (2017).
- [46] X. Zhou, W. Feng, S. Guan, B. Fu, W. Su, and Y. Yao, *J. Mater. Res.* **32**, 2993 (2017).
- [47] Y. Wu, W. Xia, W. Gao, F. Jia, P. Zhang, and W. Ren, *2D Mater.* **6**, 015018 (2018).
- [48] M. S. Hybertsen and S. G. Louie, *Phys. Rev. B* **34**, 5390 (1986).
- [49] A. V. Krukau, O. A. Vydrov, A. F. Izmaylov, and G. E. Scuseria, *J. Chem. Phys.* **125**, 224106 (2006).
- [50] W. Wei and T. Jacob, *Phys. Rev. B* **87**, 085202 (2013).
- [51] J. Sun, R. Zhang, X. Li, and J. Yang, *Appl. Phys. Lett.* **109**, 133108 (2016).
- [52] L. Yang, M. L. Cohen, and S. G. Louie, *Nano Lett.* **7**, 3112 (2007).
- [53] D. Prezzi, D. Varsano, A. Ruini, A. Marini, and E. Molinari, *Phys. Rev. B* **77**, 041404(R) (2008).
- [54] J.-H. Choi, P. Cui, H. Lan, and Z. Zhang, *Phys. Rev. Lett.* **115**, 066403 (2015).
- [55] Z. Jiang, Z. Liu, Y. Li, and W. Duan, *Phys. Rev. Lett.* **118**, 266401 (2017).
- [56] L. Sponza, H. Amara, C. Attaccalite, S. Latil, T. Galvani, F. Paleari, L. Wirtz, and F. Ducastelle, *Phys. Rev. B* **98**, 125206 (2018).
- [57] L. Schué, L. Sponza, A. Plaud, H. Bensalah, K. Watanabe, T. Taniguchi, F. Ducastelle, A. Loiseau, and J. Barjon, *Phys. Rev. Lett.* **122**, 067401 (2019).
- [58] S. Brem, A. Ekman, D. Christiansen, F. Katsch, M. Selig, C. Robert, X. Marie, B. Urbaszek, A. Knorr, and E. Malic, *Nano Lett.* **20**, 2849 (2020).
- [59] M. Feierabend, G. Berghäuser, A. Knorr, and E. Malic, *Nat. Commun.* **8**, 14776 (2017).